

Communication

A MOF-Templated Double-Shelled $\text{Co}_3\text{O}_4/\text{NiCo}_2\text{O}_4$ Nanocomposite for Electrochemical Detection of Alfuzosin

Al-Amin ¹, Gajapaneni Venkata Prasad ², Seung Joo Jang ¹, Jeong-Wook Oh ³ and Tae Hyun Kim ^{1,*}

¹ Department of Chemistry, Soonchunhyang University, Asan 31538, Republic of Korea; amin@sch.ac.kr (A.-A.); seen813@sch.ac.kr (S.J.J.)

² Department of Chemistry, Presidency University, Yelahanka, Bengaluru 560064, India; venkataprasadsvu@gmail.com

³ Department of Chemistry, Hankuk University of Foreign Studies, Yongin 17035, Republic of Korea; jeongwoh@hufs.ac.kr

* Correspondence: thkim@sch.ac.kr; Tel.: +82-41-5304722

Abstract: We developed a novel electrochemical sensor for the detection of alfuzosin (AFZ), a drug used to treat benign prostatic hyperplasia, using a double-shelled $\text{Co}_3\text{O}_4/\text{NiCo}_2\text{O}_4$ nanocomposite-modified electrode. The nanocomposites were synthesized using a template-assisted approach, with zeolitic imidazole framework-67 (ZIF-67) as the sacrificial template, involving the formation of uniform ZIF-67/Ni-Co layered double hydroxide (LDH) hollow structures followed by calcination to achieve the final nanocomposite. The nanocomposite was characterized by various techniques and showed high porosity, large surface area, and good conductivity. The nanocomposite-modified electrode exhibited excellent electrocatalytic activity towards AFZ oxidation, with a wide linear range of 5–180 μM and a low limit of detection of 1.37 μM . The sensor also demonstrated good repeatability, reproducibility, and stability selectivity in the presence of common interfering substances. The sensor was successfully applied to determine the AFZ in pharmaceutical tablets and human serum samples, with satisfactory recoveries. Our results suggest that the double-shelled $\text{Co}_3\text{O}_4/\text{NiCo}_2\text{O}_4$ nanocomposite is a promising material for the fabrication of electrochemical sensors for AFZ detection.

Keywords: metal–organic framework; ZIF-67; alfuzosin; electrochemical sensor; biological samples



Citation: Al-Amin; Prasad, G.V.; Jang, S.J.; Oh, J.-W.; Kim, T.H. A MOF-Templated Double-Shelled $\text{Co}_3\text{O}_4/\text{NiCo}_2\text{O}_4$ Nanocomposite for Electrochemical Detection of Alfuzosin. *Nanomaterials* **2024**, *14*, 757. <https://doi.org/10.3390/nano14090757>

Academic Editors: Domenica Tonelli and Yanhu Wang

Received: 28 March 2024

Revised: 22 April 2024

Accepted: 23 April 2024

Published: 25 April 2024



Copyright: © 2024 by the authors. Licensee MDPI, Basel, Switzerland. This article is an open access article distributed under the terms and conditions of the Creative Commons Attribution (CC BY) license (<https://creativecommons.org/licenses/by/4.0/>).

1. Introduction

Benign prostatic hyperplasia (BPH), a non-malignant enlargement of the prostate gland, afflicts a significant portion of the aging male population [1–3]. This condition not only hinders urinary flow but also increases the risk of bladder and urinary tract infections and even kidney damage. While various treatment options exist, alpha-adrenergic blockers remain the mainstay of BPH therapy, with alfuzosin hydrochloride (AFZ) emerging as a widely prescribed medication [4,5]. AFZ boasts potent action as a second-generation alpha1-adrenoceptor ($\alpha 1$ -AR) antagonist. Acting upon $\alpha 1$ -adrenergic receptors prevalent in the prostate and bladder neck smooth muscles, AFZ effectively relaxes these muscles, facilitating improved urine flow and alleviating BPH symptoms [6,7]. AFZ is generally well-tolerated but has potential side effects, such as dizziness, headache, and hypotension. In rare cases, more serious complications like orthostatic hypotension, priapism, and hypersensitivity reactions can occur. Given the potential for adverse effects, accurate monitoring of AFZ levels in patients becomes crucial for ensuring optimal therapeutic outcomes and minimizing risks [8].

Current analytical methods for AFZ quantification, primarily relying on chromatographic technique [9], spectrophotometry [10], spectrofluorometry [11], and capillary electrophoresis [12], often suffer from limitations like complexity, time-consuming procedures,

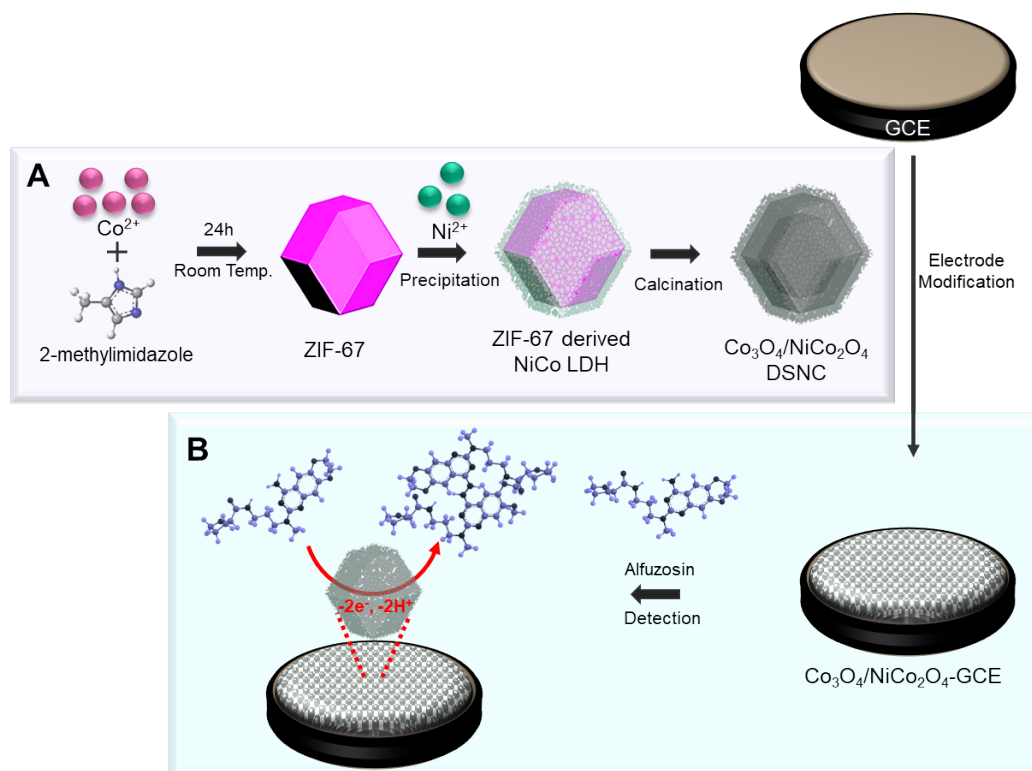
and high operational costs. To address these shortcomings, novel approaches employing highly sensitive and selective sensing platforms are actively sought.

Electrochemical methods provide a compelling alternative for AFZ detection, due to their simplicity, speed, cost-effectiveness, and sensitivity [13–19]. Electrochemical sensors operate based on the redox reactions of the analyte at the electrode surface, generating a measurable current or potential signal [20–23]. The efficacy of electrochemical sensors hinges significantly on the characteristics of electrode materials, including conductivity, surface area, catalytic activity, and stability [24–27]. Consequently, the advancement of novel electrode materials with improved electrochemical properties is vital for crafting high-performance electrochemical sensors dedicated to AFZ detection.

Metal–organic frameworks (MOFs) represent a category of porous crystalline materials consisting of metal ions or clusters linked by organic ligands [28–30]. These MOFs have garnered significant attention for diverse applications, including gas storage [31–33], separation [34–36], catalysis [37], and sensing [38–40], owing to their notable features, such as high surface area, adjustable pore size, and versatile functionality [41–43]. Additionally, MOFs can function as templates or precursors for synthesizing other nanostructures, such as metal oxides, sulfides, and carbons, through processes such as thermal decomposition [44], sulfidation [45], or carbonization [46,47]. The resulting nanostructures derived from MOFs can retain the morphology and porosity of the original MOFs while showcasing enhanced electrical and electrochemical properties. Given their tunable porosity, expansive surface area, and versatile functionality, MOFs hold great potential for advancing the field of electrochemical sensors, particularly for the detection of AFZ.

This work unveils a MOF-templated double-shelled $\text{Co}_3\text{O}_4/\text{NiCo}_2\text{O}_4$ nanocomposite specifically tailored for the electrochemical detection of AFZ. Co_3O_4 , a well-known p-type semiconductor with a tunable band gap and interesting redox behavior, offers excellent electrocatalytic potential [48,49]. Combining it with NiCo_2O_4 further enhances its physical and chemical stabilities while providing multiple oxidation states and superior electrical conductivity [50]. Additionally, designing these materials with a hollow, porous structure maximizes the abundance of active sites, facilitates rapid ion diffusion, and ultimately boosts the sensor's overall electrocatalytic performance [51]. Besides, recently, new studies demonstrate that incorporation of a nanostructured transition metal oxide into the other kind of oxide forming a double-shelled nanocage, enables the multiple redox reactions, which not only shortens ion transport pathways but also efficiently enhances the properties in specific capacitance, electrocatalytic activity and electron collection efficiency, compared with the single component one [52]. In addition, in NiCo_2O_4 , nickel and cobalt atoms exist in multiple oxidation states. This creates a special situation where electrons can easily move between these different states. Due to this mixed valence, electrons can be transferred quickly and efficiently within NiCo_2O_4 . This efficient electron movement is what makes NiCo_2O_4 a good electrical conductor. NiCo_2O_4 also exhibits excellent redox activity, meaning it can readily participate in electron transfer reactions. The unique combination of mixed valences in NiCo_2O_4 allows for easier electron movement, leading to its superior electrical conductivity compared to NiO and Co_3O_4 [53]. Scheme 1 depicts the MOF-templated double-shelled $\text{Co}_3\text{O}_4/\text{NiCo}_2\text{O}_4$ nanocomposite electrode utilized in the AFZ electrochemical sensor. The diagram illustrates the MOF template, its transformation into the double-shelled nanocomposite (Scheme 1A), and its integration into the electrode for sensitive AFZ detection (Scheme 1B). The nanocomposite was prepared by using zeolitic imidazolate framework-67 (ZIF-67), a cobalt-based MOF, as the template and precursor and introducing nickel ions (Ni^{2+}) into the ZIF-67 structure, using a precipitation method. Subsequently, the resulting ZIF-67/Ni-Co layered double hydroxide (LDH) nanocages were calcined in air to enhance their properties. Finally, the prepared double-shelled nanocomposites were drop-cast onto glassy carbon electrodes (GCEs) to fabricate $\text{Co}_3\text{O}_4/\text{NiCo}_2\text{O}_4$ -modified GCEs ($\text{Co}_3\text{O}_4/\text{NiCo}_2\text{O}_4$ -GCEs) for electrochemical sensing. The resulting nanocages are fabricated using a simple, cost-effective, and environmentally friendly method exhibit excellent performance, demonstrating improved conductivity, low

charge transfer resistance, high sensitivity, a low detection limit, excellent selectivity, reproducibility, and better stability towards the detection of AFZ [54–57]. Through this work, we present a highly efficient and robust platform for AFZ quantification. This advancement holds significant potential to revolutionize BPH management by enabling accurate and real-time monitoring of AFZ levels, ultimately contributing to improved patient safety and therapeutic efficacy.



Scheme 1. Schematic representation of (A) the synthesis of an MOF—templated double—shelled $\text{Co}_3\text{O}_4/\text{NiCo}_2\text{O}_4$ nanocomposite and (B) the fabrication of $\text{Co}_3\text{O}_4/\text{NiCo}_2\text{O}_4$ —modified glassy carbon electrode ($\text{Co}_3\text{O}_4/\text{NiCo}_2\text{O}_4$ —GCE) for AFZ electrochemical sensing.

2. Materials and Methods

2.1. Chemicals

Alfuzosin hydrochloride (AFZ), ascorbic acid (AA), uric acid (UA), glucose (glu), cobalt nitrate hexahydrate ($\text{Co}(\text{NO}_3)_2 \cdot 6\text{H}_2\text{O}$), nickel nitrate hexahydrate ($\text{Ni}(\text{NO}_3)_2 \cdot 6\text{H}_2\text{O}$), 2-methylimidazole (2-MIM), potassium hydroxide (KOH), sodium chloride (NaCl), calcium sulfate (CaSO_4), iron(II) sulfate heptahydrate ($\text{FeSO}_4 \cdot 7\text{H}_2\text{O}$), *N,N*-Dimethylformamide (DMF), human serum, sodium dihydrogen phosphate (NaH_2PO_4), and disodium hydrogen phosphate (Na_2HPO_4) were sourced from Sigma-Aldrich, United States. Methanol was procured from SK Chemicals, Republic of Korea. The tablet sample, ALFOO 10 mg, was purchased locally from pharmaceuticals in Asan, Republic of Korea. All compounds were used as received, without further purification.

The 0.05 M phosphate buffer saline (PBS) with a pH range of 5–9 was prepared by dissolving Na_2HPO_4 and NaH_2PO_4 in Millipore water and neutralizing it with 0.1 M HCl or NaOH. Millipore water was used to make all of the solutions.

2.2. Synthesis of ZIF-67

Two solutions were prepared by dissolving 100 mmol (1.455 g) of $\text{Co}(\text{NO}_3)_2 \cdot 6\text{H}_2\text{O}$ in 50 mL of methanol and 400 mmol (1.642 g) of 2-MIM in another 50 mL of methanol. Both solutions were stirred for 15 min until there was a clear solution. The 2-MIM solution was then slowly added to the $\text{Co}(\text{NO}_3)_2$ solution under vigorous stirring for 1 h at room

temperature. The resulting mixture was aged for 24 h at room temperature. The precipitated purple solid was collected by centrifugation and washed with methanol three times. The obtained product was then dried at 70 °C overnight. Finally, the dried solid was calcined in air at 350 °C for 2 h to obtain the final Co_3O_4 -MOF material.

2.3. Synthesis of $\text{Co}_3\text{O}_4/\text{NiCo}_2\text{O}_4$

A total of 188 mg of ZIF-67 templates was dispersed in 75 mL of ethanol containing 376 mg of $\text{Ni}(\text{NO}_3)_2 \cdot 6\text{H}_2\text{O}$. The mixture was stirred for 0.5 h at room temperature, leading to the formation of ZIF-67/Ni-Co LDH hollow structure particles. These particles were collected by centrifugation, washed with ethanol three times, and dried overnight at 70 °C. The as-prepared hollow structure particles were subsequently transformed into $\text{Co}_3\text{O}_4/\text{NiCo}_2\text{O}_4$ double-shelled nanocages by thermal annealing in air at 350 °C for 2 h.

2.4. Fabrication of the $\text{Co}_3\text{O}_4/\text{NiCo}_2\text{O}_4$ -Modified Electrode

Before modification, the GCE was sequentially polished with alumina powders of decreasing sizes (0.3, 0.1, and 0.05 μm) for thorough smoothening. It was then sonicated in deionized water and ethanol multiple times for deep cleaning. An amount of 1 mg of the $\text{Co}_3\text{O}_4/\text{NiCo}_2\text{O}_4$ nanocomposite was dispersed in 1 mL of DMF and homogenized by ultrasonication and vortex mixing to create a stable suspension. Subsequently, the cleaned GCE surface was coated by drop-casting 5 μL of the $\text{Co}_3\text{O}_4/\text{NiCo}_2\text{O}_4$ suspension onto its surface and drying it under an infrared lamp. The resulting modified GCE was labeled as $\text{Co}_3\text{O}_4/\text{NiCo}_2\text{O}_4$ -GCE and employed as an electrochemical sensor for detecting AFZ.

2.5. Instrumentation

The phase purity and crystal structure of the synthesized catalysts were assessed using a powder X-ray diffraction (XRD) apparatus (MiniFlex600, Rigako, Japan). Surface morphology and microstructural investigations were carried out using a field emission scanning electron microscope (FE-SEM, Sigma 500 (ZEISS, Carl Zeiss, Germany)). For more detailed microstructural properties, a transmission electron microscope (TEM, JEOL JEM-1010, JEOL Ltd., Tokyo, Japan) was employed. Electrochemical measurements were performed using a CHI 660D electrochemical workstation (CH Instruments, Inc., Austin, TX, USA, Z-202306208148 at the Research Support Center for Bio-Bigdata Analysis and Utilization of Biological Resources), employing a conventional three-electrode cell setup. The working electrodes were utilized the bare GCE and the modified GCEs, the counter electrode was a platinum wire, and the reference electrode employed was an Ag/AgCl electrode (3 M KCl).

3. Results and Discussion

3.1. Physical Characterization of the $\text{Co}_3\text{O}_4/\text{NiCo}_2\text{O}_4$ Nanocomposite

X-ray diffraction (XRD) analysis was used to investigate the crystalline structure of the materials formed at different synthesis stages. Figure 1 shows the XRD patterns of ZIF-67, ZIF/Ni-Co LDH, Co_3O_4 , and $\text{Co}_3\text{O}_4/\text{NiCo}_2\text{O}_4$. The XRD patterns of the ZIF-67 crystals in Figure 1A matched well with previously reported data [58,59]. The XRD pattern of the ZIF/NiCo-LDH composite exhibited lower peak intensities compared to ZIF-67 (Figure 1A). Similarly, the Co_3O_4 peaks in the $\text{Co}_3\text{O}_4/\text{NiCo}_2\text{O}_4$ DSNCs were weaker and broader than those observed in the Co_3O_4 NCs (Figure 1B) [60]. These observations suggest that Co_3O_4 is encapsulated within the NiCo_2O_4 shell, influencing the X-ray diffraction pattern. The patterns align well with standard data (ICDD cards No. 42-1467 for Co_3O_4 and No. 20-0781 for NiCo_2O_4), indicating the formation of spinel-structured Co and Ni oxide materials, including Co_3O_4 and NiCo_2O_4 , in the calcined samples. However, to definitively confirm the inclusion of NiCo_2O_4 , we utilized energy-dispersive X-ray spectroscopy (EDS) on the $\text{Co}_3\text{O}_4/\text{NiCo}_2\text{O}_4$ composite (Figures S2 and S3). The elemental analysis by EDS revealed the presence of Co, Ni, and O, providing conclusive evidence for the existence of NiCo_2O_4 within the material.

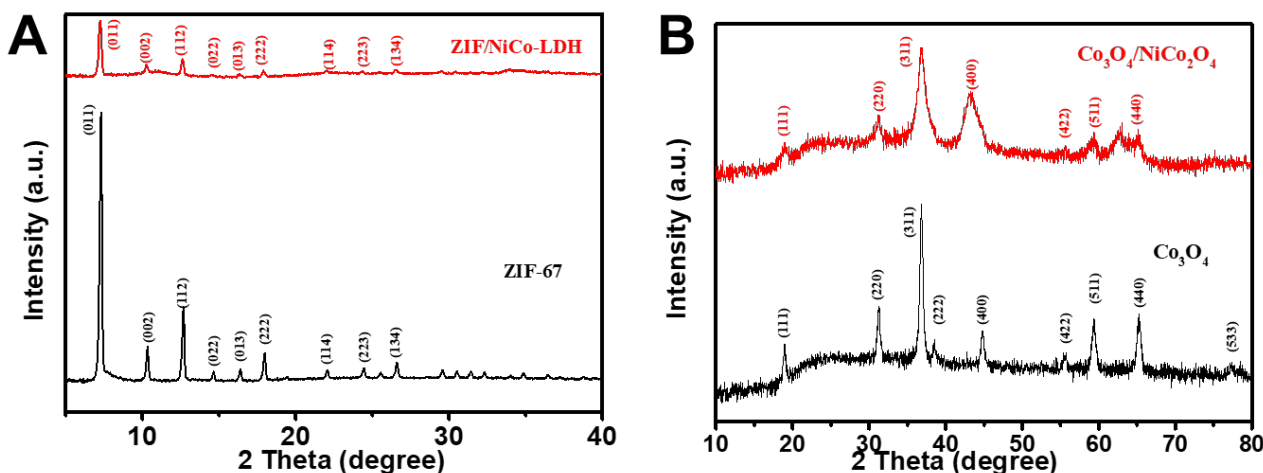


Figure 1. XRD patterns of (A) ZIF-67 and ZIF/Ni-Co LDH and (B) Co_3O_4 and $\text{Co}_3\text{O}_4/\text{NiCo}_2\text{O}_4$.

X-ray photoelectron spectroscopy (XPS) was employed to investigate the chemical composition of $\text{Co}_3\text{O}_4/\text{NiCo}_2\text{O}_4$ DSNCs in more detail (Figure S1). The survey spectrum (Figure S1A) confirmed the presence of nickel (Ni), cobalt (Co), and oxygen (O). Additionally, it revealed trace amounts of carbon (C), likely from the reference material, and no other impurities were detected. The Ni 2p spectrum (Figure S1B) was analyzed using a Gaussian fitting method. This method identified two spin-orbit doublets along with two shake-up satellites, indicating the presence of both Ni^{2+} and Ni^{3+} ions. Fitting peaks at 854.1 eV and 872.8 eV were assigned to Ni^{2+} , while those at 856.3 eV and 874.5 eV were attributed to Ni^{3+} [61]. Similar results were obtained for the Co 2p spectrum (Figure S1C). Here, the fitting peaks at 778.7 eV and 794.7 eV were assigned to Co^{2+} , while the peaks at 774.9 eV and 793.2 eV were attributed to Co^{3+} [62]. The Gaussian fitting of the O 1s spectrum (Figure S1D) revealed the presence of three distinct oxygen species labeled O1, O2, and O3. Based on previous studies, O1 at a binding energy of 529.22 eV is characteristic of a metal–oxygen bond [63]. O2, with a binding energy of 531.0 eV, is commonly associated with defects in the material that have low oxygen coordination [64]. Finally, O3 at 532.0 eV is attributed to a combination of physically and chemically adsorbed water molecules on the surface [65,66]. Thus, the XPS analysis suggests that the surface of the synthesized NiCo_2O_4 contains Ni^{2+} , Ni^{3+} , Co^{2+} , and Co^{3+} ions. The presence of these abundant intrinsic redox couples, $\text{Ni}^{2+}/\text{Ni}^{3+}$ and $\text{Co}^{2+}/\text{Co}^{3+}$, is expected to provide the porous $\text{Co}_3\text{O}_4/\text{NiCo}_2\text{O}_4$ DSNCs with a large number of electroactive sites.

The surface morphology and crystal shape of the samples were examined by FESEM and TEM analyses (Figure 2). The ZIF-67 nanoparticles exhibited a polyhedral structure characterized by a smooth surface [67–69], as depicted in Figure 2A,E. Upon undergoing a reaction with $\text{Ni}(\text{NO}_3)_2 \cdot 6\text{H}_2\text{O}$ and an ethanol solution for 0.5 h, the particles maintained their polyhedral morphology, but their surfaces became slightly rough, as shown in Figure 2B. Moreover, TEM analysis revealed that the particle surfaces were not as smooth as those of the original ZIF-67 (Figure 2F). Notably, the inner structure of ZIF-67/Ni-Co LDH was porous, consisting of interconnected nanosheets of LDH. FESEM and TEM revealed the complete removal of the ZIF-67 cores, resulting in fully hollow Ni-Co LDH nanocages (NCs). To achieve the decomposition of ZIF/Ni-Co LDH and form the desired Co–Ni oxides, calcination was performed at 350 °C. Pristine ZIF-67 was also calcined under identical conditions for comparison. Thermal annealing of ZIF-67 crystals and Ni-Co LDH is known to produce spinel-type Co_3O_4 and NiCo_2O_4 , respectively. Notably, both annealed materials exhibited cage-like structures, enabling the formation of double-shelled nanocages (DSNCs) through the calcination of ZIF-67/Ni-Co LDH hollow structures. The Co_3O_4 particles derived from ZIF-67 displayed sharp convex shapes after calcination (Figure 2C). Importantly, these Co_3O_4 particles possessed a hollow cage-like structure (Figure 2G). In contrast, particles derived from ZIF/Ni-Co LDH exhibited a

polyhedral morphology, with a rougher surface and a confirmed double-shell structure mirroring their parent structures. However, compared to their hollow precursors, the significantly more open interiors of the $\text{Co}_3\text{O}_4/\text{NiCo}_2\text{O}_4$ particles resulted in morphologies closer to true double-shelled nanocages with well-defined voids. The presence of numerous nano-/micro-scale gaps between adjacent nanoparticles indicated that the synthesized $\text{Co}_3\text{O}_4/\text{NiCo}_2\text{O}_4$ DSNCs were highly porous. Energy-dispersive X-ray spectroscopy (EDS) analysis confirmed the chemical composition of the $\text{Co}_3\text{O}_4/\text{NiCo}_2\text{O}_4$ DSNCs, with the expected elements (O, Co, and Ni) detected (Figures S2 and S3), corroborating the expected composition of $\text{Co}_3\text{O}_4/\text{NiCo}_2\text{O}_4$ DSNCs.

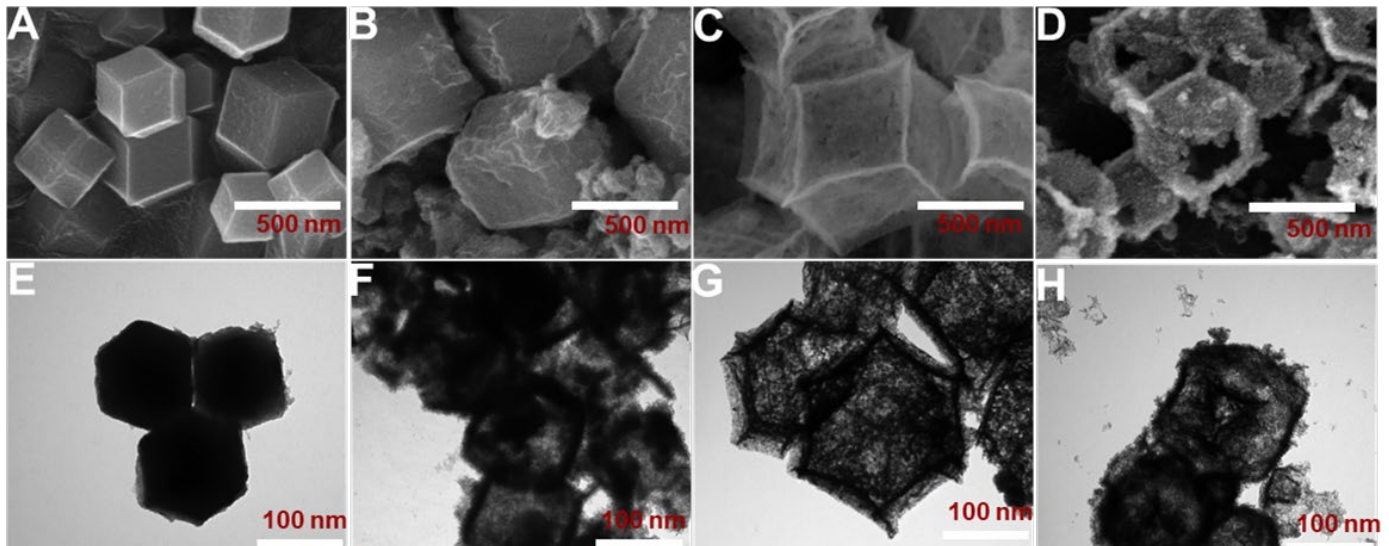


Figure 2. FESEM (A–D) and TEM (E–H) images of ZIF-67, ZIF/Ni-Co LDH, Co_3O_4 , and $\text{Co}_3\text{O}_4/\text{NiCo}_2\text{O}_4$.

3.2. Electrochemical Characterization of $\text{Co}_3\text{O}_4/\text{NiCo}_2\text{O}_4$ -GCE

Electrochemical analysis revealed a superior performance for $\text{Co}_3\text{O}_4/\text{NiCo}_2\text{O}_4$ electrodes modified on glassy carbon electrodes (GCEs). Cyclic voltammetry (CV) in a 1 mM $[\text{Fe}(\text{CN})_6]^{3-}/0.1$ M KCl solution (Figure 3A) showcased significantly enhanced redox behavior, compared to bare GCE and Co_3O_4 -GCE. $\text{Co}_3\text{O}_4/\text{NiCo}_2\text{O}_4$ -GCE displayed a larger peak current response (20.6 μA) and a substantially lower peak-to-peak separation potential ($\Delta E_p = 0.071$ V), compared to other electrodes. These observations highlight improved electron transfer kinetics facilitated by Ni incorporation and the porous/hollow nanocomposite structure. This suggests a greater ease of redox reactions on $\text{Co}_3\text{O}_4/\text{NiCo}_2\text{O}_4$ electrodes. The conductivity and electron mobility of each modified electrode were examined through electrochemical impedance spectroscopy (EIS). Figure 3B depicts the EIS spectra of bare GCE, Co_3O_4 -GCE, and $\text{Co}_3\text{O}_4/\text{NiCo}_2\text{O}_4$ -GCE in a 1 mM $[\text{Fe}(\text{CN})_6]^{3-}$ solution containing 0.1 M KCl. An applied amplitude potential of 0.005 V and a frequency range of 1 Hz–100 kHz were employed. The diameter of the semicircle in the Nyquist plot corresponded to the R_{ct} value, indicating the kinetics of electron transfer at the electrode/electrolyte interface. EIS analysis unraveled the improved electron transfer kinetics of $\text{Co}_3\text{O}_4/\text{NiCo}_2\text{O}_4$ electrodes due to enhanced conductivity. Figure 4B showcases the EIS spectra, revealing a significantly lower charge transfer resistance (R_{ct}) for $\text{Co}_3\text{O}_4/\text{NiCo}_2\text{O}_4$ -GCE (140 Ω), compared to bare GCE (390 Ω) and Co_3O_4 -GCE (497 Ω). This decrease in R_{ct} , visualized by the smaller semicircle diameter in the Nyquist plot, indicates a faster electron transfer at the electrode/electrolyte interface. Interestingly, Co_3O_4 -GCE exhibited a higher R_{ct} , suggesting impeded electron transport, likely due to the poor conductivity of Co_3O_4 . In contrast, incorporating Ni into the composite significantly boosted conductivity (evidenced by the lower R_{ct}) thanks to Ni's inherent conductivity and the porous/hollow nanocomposite structure that facilitates electrolyte ion diffusion. Therefore, the synergistic

effect of Ni and the nanocomposite architecture empower $\text{Co}_3\text{O}_4/\text{NiCo}_2\text{O}_4$ electrodes with superior electron transfer capabilities. CV analysis at varying scan rates revealed diffusion-controlled kinetics for the redox reaction of $[\text{Fe}(\text{CN})_6]^{3-}$ at $\text{Co}_3\text{O}_4/\text{NiCo}_2\text{O}_4$ -GCE. Figure 3C shows a progressive increase in redox peak currents (I_{pa} and I_{pc}) with increasing scan rates (20–200 mV s^{-1}), confirming this behavior. The linear relationship between the square root of the scan rate (ν) and peak currents (Figure 3D) further strengthens this conclusion. Notably, $\text{Co}_3\text{O}_4/\text{NiCo}_2\text{O}_4$ -GCE exhibited significantly higher peak currents, compared to bare GCE and Co_3O_4 -GCE (Figure S4). Electrochemical active surface area (EASA) calculations, based on the Randles–Sevcik equation, confirmed $\text{Co}_3\text{O}_4/\text{NiCo}_2\text{O}_4$ -GCE's superior electrocatalytic activity. With an EASA of 0.0997 cm^2 , it surpassed both Co_3O_4 -GCE (0.0655 cm^2) and bare GCE (0.0697 cm^2). This larger EASA, coupled with lower resistance and a smaller peak separation observed in $\text{Co}_3\text{O}_4/\text{NiCo}_2\text{O}_4$ -GCE, collectively point towards its enhanced ability to sense AFZ.

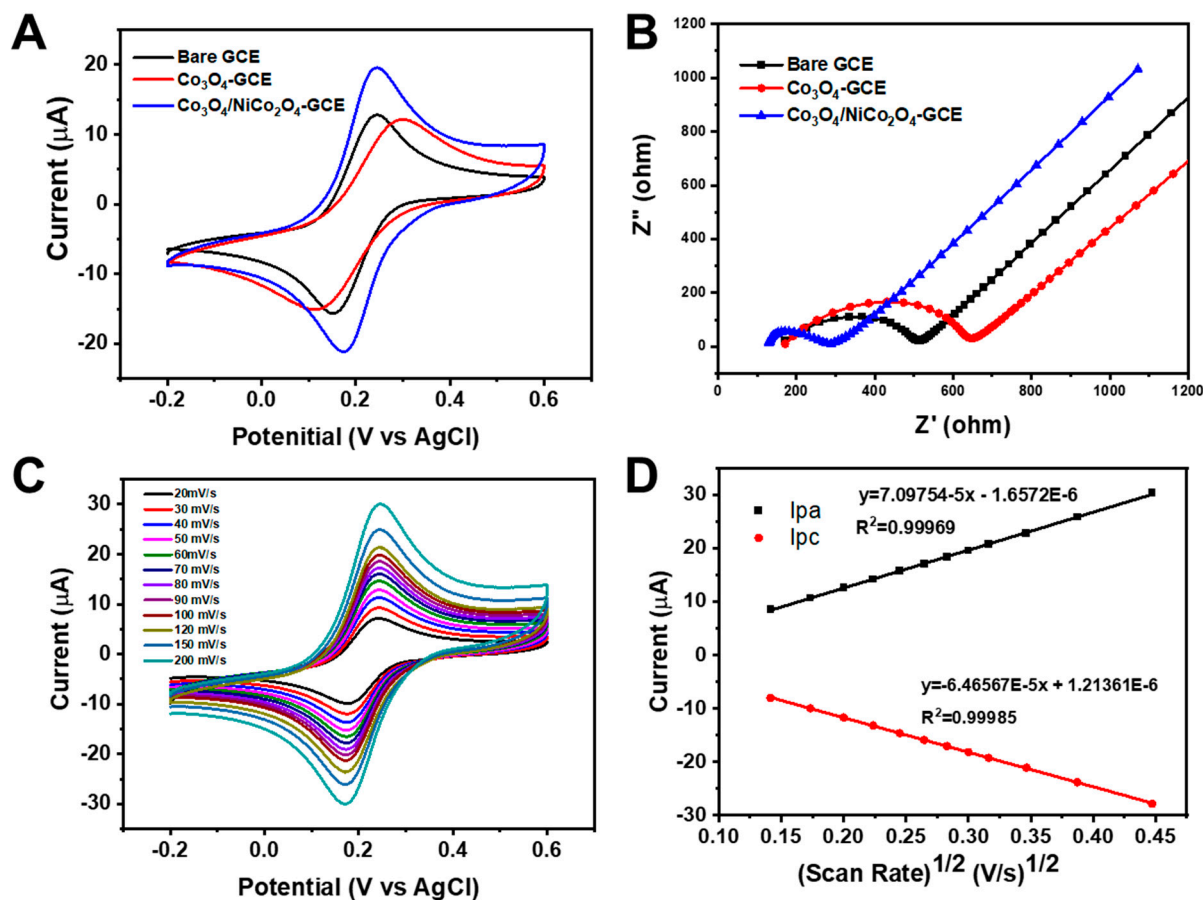


Figure 3. (A) CV curves at the scan rate of 100 mV s^{-1} and (B) Nyquist plots of bare GCE, Co_3O_4 -GCE, and $\text{Co}_3\text{O}_4/\text{NiCo}_2\text{O}_4$ -GCE in 0.1 M KCl with $1 \text{ mM } [\text{Fe}(\text{CN})_6]^{3-}$. (C) CV curves at various scan rates from 20 to $200 \times 10^3 \text{ V s}^{-1}$ at $\text{Co}_3\text{O}_4/\text{NiCo}_2\text{O}_4$ -GCE and (D) the corresponding linear plots of $\nu^{1/2}$ vs. redox peak currents ($I_{\text{pa}}/I_{\text{pc}}$).

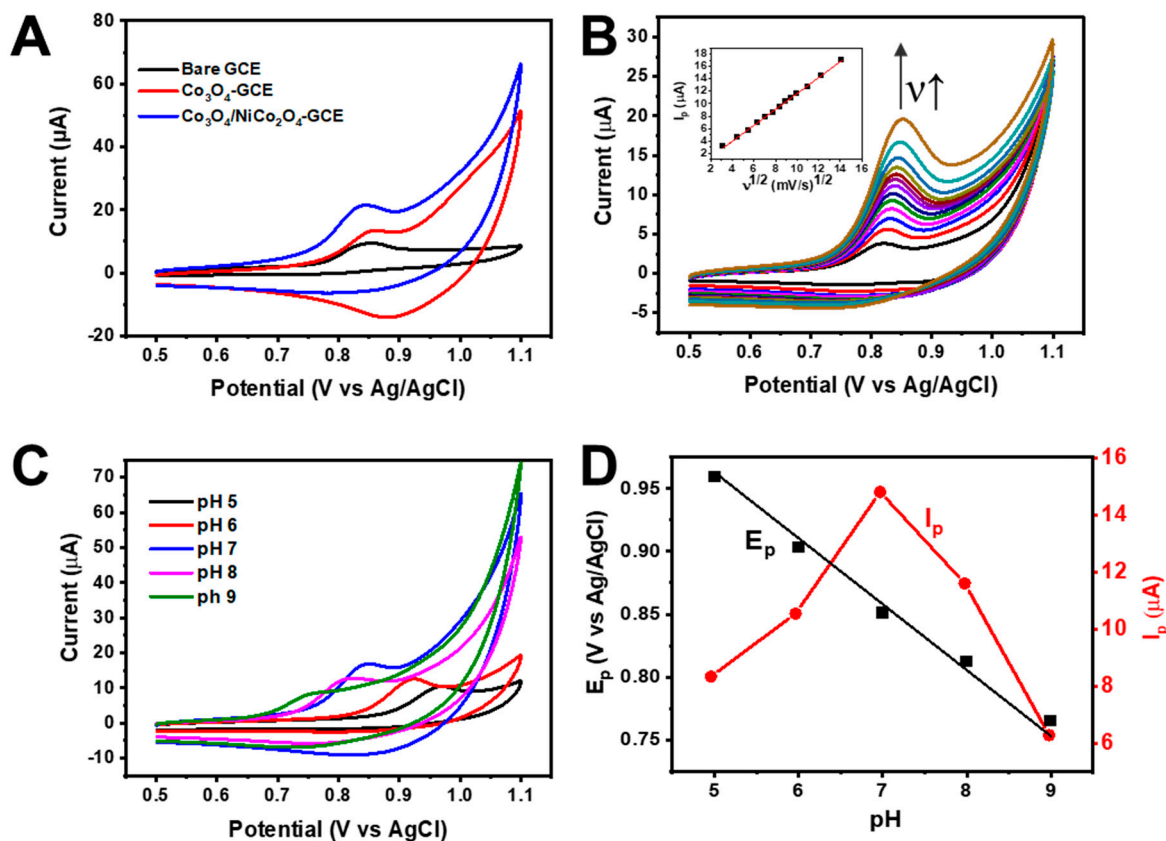


Figure 4. (A) CV curves recorded on bare GCE, Co_3O_4 -GCE and $\text{Co}_3\text{O}_4/\text{NiCo}_2\text{O}_4$ -GCE in 0.05 M PBS (pH 7) in the presence of 100 μM AFZ at a scan rate of 100 mV/s. (B) CV curves recorded on $\text{Co}_3\text{O}_4/\text{NiCo}_2\text{O}_4$ -GCE in 0.05 M PBS (pH 7) in the presence of 100 μM AFZ at increasing scan rates from 10 to 200 mV/s. (C) CVs of 100 μM AFZ at $\text{Co}_3\text{O}_4/\text{NiCo}_2\text{O}_4$ -GCE in various pH (5 to 9) solutions. (D) Peak potential versus pH (black square and line) and peak current versus pH (red circle and line) at $\text{Co}_3\text{O}_4/\text{NiCo}_2\text{O}_4$ -GCE in the presence of 100 μM AFZ at a scan rate of 100 mV/s.

3.3. Electrochemical Activity of $\text{Co}_3\text{O}_4/\text{NiCo}_2\text{O}_4$ -GCE toward AFZ

To comprehensively elucidate the electrochemical behavior of the $\text{Co}_3\text{O}_4/\text{NiCo}_2\text{O}_4$ -GCE sensor for AFZ detection, we systematically investigated the impacts of key parameters, such as electrode modifier, scan rate, and pH. This approach, coupled with the inherent high electrical conductivity of the composite, aimed to establish its suitability for AFZ sensing. Figure 4A shows the CV curves of bare GCE, Co_3O_4 -GCE, and $\text{Co}_3\text{O}_4/\text{NiCo}_2\text{O}_4$ -GCE in 0.05 M PBS (pH 7.0) containing 0.1 mM AFZ at a scan rate of 100 mV s⁻¹. The bare GCE displayed a significantly lower oxidation peak current ($I_{pa} = 6.52 \mu\text{A}$), compared to both of the modified electrodes, highlighting limitations in electron transfer. In contrast, $\text{Co}_3\text{O}_4/\text{NiCo}_2\text{O}_4$ -GCE exhibited a pronounced enhancement in I_{pa} (15.6 μA), demonstrating the significant role of Ni incorporation in promoting electron conductivity. This enhancement likely stems from a synergistic effect: (1) the inherent conductivity of Ni and (2) the increased EASA offered by the unique double-shelled, hollow, and porous structure of $\text{Co}_3\text{O}_4/\text{NiCo}_2\text{O}_4$. This synergism ultimately translates to the observed amplification of the AFZ oxidation peak current. To understand the underlying electrochemical kinetics of AFZ oxidation at the $\text{Co}_3\text{O}_4/\text{NiCo}_2\text{O}_4$ -GCE sensor, we investigated the impact of scan rate using CV. In Figure 4B, CV curves corresponding to various scan rates (v) ranging from 10 to 200 mV s⁻¹ are presented, with measurements conducted in a solution containing 100 μM AFZ dissolved in 0.05 M PBS at pH 7. The oxidation peak current (I_p) progressively increased with a higher v . Further analysis revealed a linear relationship between I_{pa} and the square root of the scan rate ($v^{1/2}$) (inset of Figure 4B). The resulting fit

yielded the equation $I_p (\mu\text{A}) = 1.28 (v^{1/2}) - 1.20$ ($R^2 = 0.9992$). This empirical relationship strongly supports the assertion that the electro-oxidation of AFZ at the $\text{Co}_3\text{O}_4/\text{NiCo}_2\text{O}_4$ -GCE surface is predominantly controlled by the diffusion process. The pH of the solution significantly affects both the behavior of the analyte and the rate of electron transport towards the electrode, playing a crucial role in optimizing the sensor's performance. To elucidate this influence, we investigated the impact of pH on the electrochemical response of 100 μM AFZ using $\text{Co}_3\text{O}_4/\text{NiCo}_2\text{O}_4$ -GCE sensors with CV at various pH levels (5.0 to 9.0) and a scan rate of 100 mV s^{-1} . Figure 4C illustrates the intriguing relationship between pH and the electrochemical response. Notably, the plot of the oxidation peak potential (E_p) against pH (Figure 4D black square and line) revealed a linear correlation, expressed by the equation $E_p = -0.053\text{pH} + 1.23$, with an R^2 value of 0.99. The comparable slope value to the Nernstian theoretical value of -0.059 V against the pH [70] indicates that the electro-oxidation of AFZ involves an equal number of electrons and protons. These consistent findings align with the proposed mechanism of the AFZ electro-oxidation reaction, as depicted in Scheme 1B. As illustrated in Figure 4D (red circle and line), the peak current intensity exhibited a discernible increase as the electrolyte pH rose from 5.0 to 7.0, followed by a subsequent decrease from pH 7.0 to pH 9.0. The peak current showed the highest AFZ oxidation peak current at pH 7.0, which was consequently employed throughout the experimental procedures.

3.4. Electrochemical Sensing Performance

The DPV method, known for its simplicity, wide linear response range, excellent sensitivity, and low limit of detection (LOD), was employed to assess the electrochemical activity of $\text{Co}_3\text{O}_4/\text{NiCo}_2\text{O}_4$ -GCE for AFZ oxidation. This investigation was conducted at varying concentrations of AFZ in 0.05 M PBS (pH 7), as shown in Figure 5A. The anodic peak current (I_{pa}) of AFZ exhibited a gradual increase with rising AFZ concentrations, ranging from 5 to 180 μM . The calibration plot depicting the relationship between AFZ concentrations (ranging from 0.5 to 180 μM) and the anodic peak current (I_{pa}) is presented in Figure 5B, revealing two distinct linear regions. Lower AFZ concentrations caused a faster response, likely attributable to the rapid transfer of molecules to the electrode surface. Conversely, higher concentrations caused a slower response. This discrepancy in response rates elucidates the presence of the two distinct linear regions in the calibration plot. The resulting linear plots of I_{pa} and AFZ concentrations are written as $I_{pa} (\mu\text{A}) = 0.134 C [\mu\text{M}] + 6.82$ ($R^2 = 0.993$) (5–40 μM) and $I_{pa} (\mu\text{A}) = 0.0567 C [\mu\text{M}] + 4.14$ ($R^2 = 0.975$) (40–180 μM), suggesting the modified electrode has excellent sensitivity for AFZ oxidation. The limit of detection (LOD) for the sensor was determined to be 1.37 μM , calculated using the formula ($\text{LOD} = 3S/m$), where S is the standard deviation of the blank response, and m is the slope of the calibration curve [71]. A comparative analysis of this sensor with other previously reported AFZ sensors is presented in Table 1. In practical applications, assessing the interference from excipients, including common biological metabolites and inorganic compounds, is crucial for AFZ detection. To assess the selectivity of our sensor for AFZ detection, we investigated the influence of common biological metabolites (ascorbic acid, AA, Glu, and UA) and inorganic compounds (K^+ , Na^+ , NO_3^- , Co^{3+} , SO_4^{2-} , Ca^{2+} , Fe^{2+} , and Cl^-) using DPV. These potential interferences were added in a 20-fold excess to a solution containing 100 μM AFZ in 0.05 M PBS (pH 7.0). The sensor exhibited minimal changes in the peak potential upon the addition of these species, indicating negligible interference with AFZ detection. The bar graph depicting the oxidation current response to different interfering species showed a relative error below 10% (Figure 5C), confirming the $\text{Co}_3\text{O}_4/\text{NiCo}_2\text{O}_4$ -GCE sensor's high selectivity for AFZ.

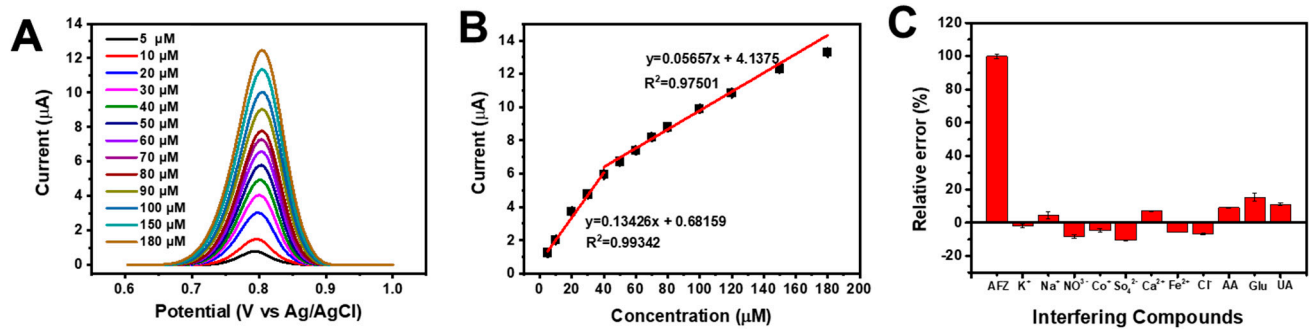


Figure 5. (A) DPV curves and (B) the corresponding plot of the anodic peak current (I_{pa}) versus the AFZ concentration for the $\text{Co}_3\text{O}_4/\text{NiCo}_2\text{O}_4$ -GCE obtained at various AFZ concentrations, ranging from 5 to 180 μM in the presence of 0.05 M PBS (pH 7). (C) The bar plot of oxidation peak currents vs. interfering species. [AFZ] = 100 μM and [Interferences] = 2 mM.

Table 1. Comparison of the linear range and LOD for AFZ detection using various methods.

Method		Linear Range (μM)	LOD (μM)	Ref.
Potentiometry using modified electrodes	Electrode I	10–10,000	9.6	[54]
	Electrode II	10–10,000	9.7	
RP-HPLC		-	8.014	[55]
Colorimetry		25–300	6.13	[56]
DPV		0.02–90	0.0041	[57]
Amperometry	MWCNT/CLIE	10–100	2.5	
DPV using $\text{Co}_3\text{O}_4/\text{NiCo}_2\text{O}_4$ -GCE		5–180	1.37	This work

3.5. Effect of Repeatability, Reproducibility, and Stability

The reliability and practical applicability of the sensor hinge on its repeatability, reproducibility, and stability. The proposed sensor exhibited outstanding repeatability, as evidenced by the voltammetric responses in Figure 6A, which showed negligible variation across five distinct measurements. Similarly, Figure 6B demonstrates the sensor's commendable reproducibility, with consistent voltammetric responses from five separately produced electrodes. The sensor's excellent long-term stability is evident in Figure 6C, showing a sustained peak current of 92.0% of its initial value after 20 days of storage at room temperature, with measurements taken every 5 days. These findings underscore the reliable performance that can be attained through this fabrication technique.

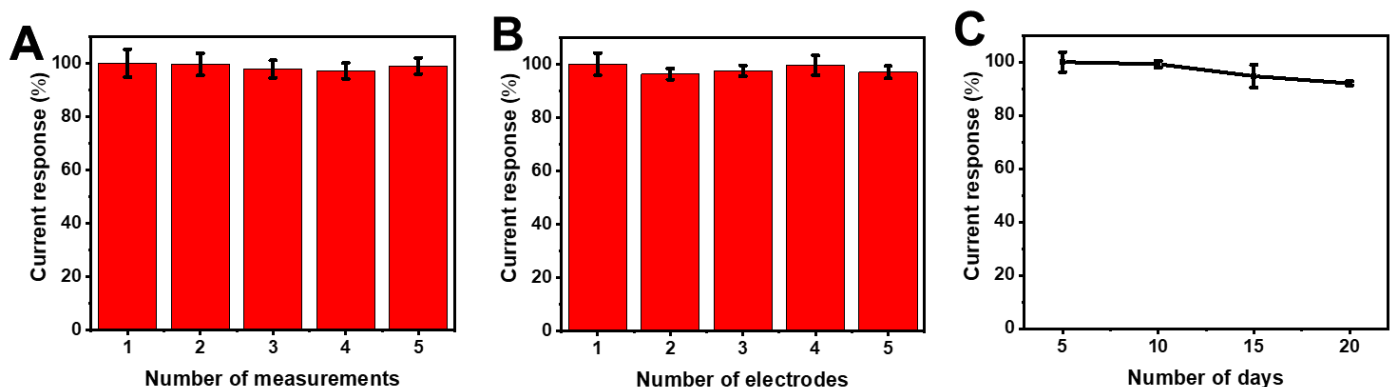


Figure 6. (A) Repeatability of the sensor for five different measurements. The current was measured in triplicate ($n = 3$). (B) Reproducibility of the sensor for five different fabricated electrodes. The current was measured in triplicate ($n = 3$). (C) Stability of the sensor in twenty days.

3.6. Detection of AFZ in Real Samples

To validate the applicability of our proposed sensing system for real-world AFZ detection, we investigated its performance using real samples. We prepared a real sample matrix using 0.05 M PBS (pH 7.0) to human serum (AFZ-free) and spiked it with varying concentrations of AFZ-containing pharmaceutical tablets. The results, presented in Table 2, demonstrated excellent recovery rates and low RSD values, indicating the promising potential of our proposed sensing strategy for real-world applications.

Table 2. Detection of AFZ concentrations in real samples using Co₃O₄/NiCo₂O₄-GCE (*n* = 3).

Samples	Added (μM)	Found (μM)	Recovery (%)	RSD (%)
Tablet	15	14.84	98.93	0.87
	25	24.81	99.23	0.82
	35	34.09	97.41	1.14
Human Serum	15	14.54	96.95	2.92
	20	19.86	99.28	1.59
	25	24.90	99.60	0.81

4. Conclusions

In summary, our study introduces a novel electrochemical sensor based on an MOF-templated, double-shelled Co₃O₄/NiCo₂O₄ nanocomposite for the detection of alfuzosin (AFZ), a medication widely used for treating benign prostatic hyperplasia (BPH). The nanocomposite was synthesized via a template-assisted approach, demonstrating high porosity, large surface area, and good conductivity—properties ideal for electrochemical sensing. The sensor exhibited excellent electrocatalytic activity towards AFZ oxidation, with a wide linear detection range (5–180 μM) and a low limit of detection (1.37 μM). Furthermore, the sensor displayed good repeatability, reproducibility, stability, and selectivity, even in the presence of common interfering substances. The applicability of the sensor was validated through the successful determination of AFZ in pharmaceutical tablets and human serum samples, achieving satisfactory recovery rates. These findings highlight the double-shelled Co₃O₄/NiCo₂O₄ nanocomposite as a promising material for the development of efficient electrochemical sensors for AFZ detection.

Supplementary Materials: The following supporting information can be downloaded at: <https://www.mdpi.com/article/10.3390/nano14090757/s1>, Figure S1. (A) XPS survey spectrums of Co₃O₄/NiCo₂O₄ DSNCs; XPS spectra of (B) Ni 2p, (C) Co 2p, and (D) O 1s. Figure S2. EDS spectrum of Co₃O₄/NiCo₂O₄. Figure S3. EDS mapping analysis of the Co₃O₄/NiCo₂O₄ DSNCs nanocomposite. Figure S4. CV curves at various scan rates from 20 to 200 mV/s at (A) bare GCE and (C) Co₃O₄-GCE. Linear plots of $v^{1/2}$ vs. redox peak currents (I_{pa}/I_{pc}) at (B) bare GCE and (D) Co₃O₄-GCE in 1 mM [Fe(CN)₆]³⁻ in 0.1M KCl solution.

Author Contributions: Conceptualization, A.-A. and G.V.P.; methodology, T.H.K.; software, A.-A. and T.H.K.; validation A.-A. and J.-W.O.; formal analysis, A.-A. and S.J.J.; investigation, A.-A.; resources, T.H.K.; data curation, A.-A.; writing—original draft preparation, T.H.K.; writing—review and editing, T.H.K. and S.J.J.; visualization, A.-A. and T.H.K.; supervision, T.H.K.; project administration, T.H.K.; funding acquisition, T.H.K. All authors have read and agreed to the published version of the manuscript.

Funding: This work was financially supported by the National Research Foundation of Korea (NRF) grants (NRF-2020R1A2C1014918, NRF-2021R1A6A1A03039503), the Korea Innovation Foundation grant (2023-DD-UP-0007) funded by the Ministry of Science and ICT (MSIT), and the Korea Basic Science Institute (National Research Facilities and Equipment Center) grant (2022R1A6C101B794) funded by the Ministry of Education (MOE). This work was also supported by the Soonchunhyang University research fund.

Data Availability Statement: Data are contained within the article and Supplementary Materials.

Conflicts of Interest: The authors declare no conflicts of interest.

References

1. Barry, M.J.; Roehrborn, C.G. Benign Prostatic Hyperplasia. *BMJ* **2001**, *323*, 1042–1046. [[CrossRef](#)] [[PubMed](#)]
2. Chughtai, B.; Forde, J.C.; Thomas, D.D.M.; Laor, L.; Hossack, T.; Woo, H.H.; Te, A.E.; Kaplan, S.A. Benign Prostatic Hyperplasia. *Nat. Rev. Dis. Primer* **2016**, *2*, 1–15. [[CrossRef](#)] [[PubMed](#)]
3. Kim, E.H.; Larson, J.A.; Andriole, G.L. Management of Benign Prostatic Hyperplasia. *Annu. Rev. Med.* **2016**, *67*, 137–151. [[CrossRef](#)] [[PubMed](#)]
4. Roehrborn, C.G.; ALTESS Study Group. Alfuzosin 10 Mg Once Daily Prevents Overall Clinical Progression of Benign Prostatic Hyperplasia but Not Acute Urinary Retention: Results of a 2-year Placebo-controlled Study. *BJU Int.* **2006**, *97*, 734–741. [[CrossRef](#)] [[PubMed](#)]
5. MacDonald, R.; Wilt, T.J. Alfuzosin for Treatment of Lower Urinary Tract Symptoms Compatible with Benign Prostatic Hyperplasia: A Systematic Review of Efficacy and Adverse Effects. *Urology* **2005**, *66*, 780–788. [[CrossRef](#)] [[PubMed](#)]
6. Mehik, A.; Alas, P.; Nickel, J.C.; Sarpola, A.; Helström, P.J. Alfuzosin Treatment for Chronic Prostatitis/Chronic Pelvic Pain Syndrome: A Prospective, Randomized, Double-Blind, Placebo-Controlled, Pilot Study. *Urology* **2003**, *62*, 425–429. [[CrossRef](#)] [[PubMed](#)]
7. De la Rosette, J.; Karthaus, H.F.M.; van Kerrebroeck, P.E.; de Boo, T.; Debruyne, F.M.J. Research in ‘Prostatitis Syndromes’: The Use of Alfuzosin (a New α (1)-Receptor-Blocking Agent) in Patients Mainly Presenting with Micturition Complaints of an Irritative Nature and Confirmed Urodynamic Abnormalities. *Eur. Urol.* **1992**, *22*, 222–227. [[CrossRef](#)]
8. Siroosbakht, S.; Rezakhaniha, S.; Namdari, F.; Rezakhaniha, B. Is There Relationship between Serum Uric Acid Levels and Lower Urinary Tract Symptoms, Prostate Volume, and PSA in Men without Cancer? A Prospective Population-Based Study. *Andrologia* **2021**, *53*, e14200. [[CrossRef](#)] [[PubMed](#)]
9. Wiesner, J.L.; Sutherland, F.C.W.; Van Essen, G.H.; Hundt, H.K.L.; Swart, K.J.; Hundt, A.F. Selective, Sensitive and Rapid Liquid Chromatography–Tandem Mass Spectrometry Method for the Determination of Alfuzosin in Human Plasma. *J. Chromatogr. B* **2003**, *788*, 361–368. [[CrossRef](#)] [[PubMed](#)]
10. Ashour, S.; Chehna, M.F.; Bayram, R. Spectrophotometric Determination of Alfuzosin HCl in Pharmaceutical Formulations with Some Sulphonephthalein Dyes. *Int. J. Biomed. Sci.* **2006**, *2*, 273. [[CrossRef](#)]
11. Karasakal, A.; Ulu, S.T. Sensitive Spectrofluorimetric Determination of Alfuzosin in Pharmaceutical Preparations and Human Urine Using Dansyl Chloride. *J. Anal. Chem.* **2015**, *70*, 708–711. [[CrossRef](#)]
12. Belal, F.; Walash, M.; Fathy, M.; Zayed, S.; Borg, H. Sensitive Analysis of Five Alpha Blockers in Dosage Forms and Human Plasma by Field Amplified Sample Injection Combined with Micellar Electrokinetic Chromatography. *Microchem. J.* **2019**, *146*, 1173–1180. [[CrossRef](#)]
13. Hayat, M.; Shah, A.; Nisar, J.; Shah, I.; Haleem, A.; Ashiq, M.N. A Novel Electrochemical Sensing Platform for the Sensitive Detection and Degradation Monitoring of Methylene Blue. *Catalysts* **2022**, *12*, 306. [[CrossRef](#)]
14. Lopes, L.C.; Santos, A.; Bueno, P.R. An Outlook on Electrochemical Approaches for Molecular Diagnostics Assays and Discussions on the Limitations of Miniaturized Technologies for Point-of-Care Devices. *Sens. Actuators Rep.* **2022**, *4*, 100087. [[CrossRef](#)]
15. Hu, Q.; Wan, J.; Wang, H.; Cao, X.; Li, S.; Liang, Y.; Luo, Y.; Wang, W.; Niu, L. Boronate-Affinity Cross-Linking-Based Ratiometric Electrochemical Detection of Glycoconjugates. *Anal. Chem.* **2022**, *94*, 9481–9486. [[CrossRef](#)] [[PubMed](#)]
16. Yang, H.; Liu, Z.; Liu, C.; Zhang, Y. FeMoO₄ Nanospheres-Based Nanozymatic Colorimetry for Rapid and Sensitive Pyrophosphate Detection. *J. Mater. Chem. B* **2022**, *10*, 321–327. [[CrossRef](#)] [[PubMed](#)]
17. Agrahari, S.; Gautam, R.K.; Singh, A.K.; Tiwari, I. Nanoscale Materials-Based Hybrid Frameworks Modified Electrochemical Biosensors for Early Cancer Diagnostics: An Overview of Current Trends and Challenges. *Microchem. J.* **2022**, *172*, 106980. [[CrossRef](#)]
18. Singh, S.; Gill, A.A.; Nlooto, M.; Karpoornath, R. Prostate Cancer Biomarkers Detection Using Nanoparticles Based Electrochemical Biosensors. *Biosens. Bioelectron.* **2019**, *137*, 213–221. [[CrossRef](#)] [[PubMed](#)]
19. Rojas, D.; Della Pelle, F.; Del Carlo, M.; Escarpa, A.; Compagnone, D. Nanomaterial-Based Electrochemical Sensing Strategies for Cell Lines Oxidative Stress Evaluation and for Bio-Compounds Detection in Food. In Proceedings of the 2nd European Biosensor Symposium 2019, Florence, Italy, 18–21 February 2019.
20. Grieshaber, D.; MacKenzie, R.; Vörös, J.; Reimhult, E. Electrochemical Biosensors—Sensor Principles and Architectures. *Sensors* **2008**, *8*, 1400–1458. [[CrossRef](#)] [[PubMed](#)]
21. Islam, M.N.; Channon, R.B. Electrochemical Sensors. In *Bioengineering Innovative Solutions for Cancer*; Elsevier: Amsterdam, The Netherlands, 2020; pp. 47–71.
22. Kimmel, D.W.; LeBlanc, G.; Meschievitz, M.E.; Cliffel, D.E. Electrochemical Sensors and Biosensors. *Anal. Chem.* **2012**, *84*, 685–707. [[CrossRef](#)] [[PubMed](#)]
23. D’Orazio, P.; Meyerhoff, M.E. Electrochemistry and Chemical Sensors. In *Tietz Fundamentals of Clinical Chemistry and Molecular Diagnostics*; Elsevier: Amsterdam, The Netherlands, 2014; Volume 151.
24. Lee, Y.-Y.; Sriram, B.; Wang, S.-F.; Kogularasu, S.; Chang-Chien, G.-P. A Comprehensive Review on Emerging Role of Rare Earth Oxides in Electrochemical Biosensors. *Microchem. J.* **2023**, *193*, 109140. [[CrossRef](#)]
25. Chen, Y.; Yang, Z.; Hu, H.; Zhou, X.; You, F.; Yao, C.; Liu, F.J.; Yu, P.; Wu, D.; Yao, J. Advanced Metal–Organic Frameworks-Based Catalysts in Electrochemical Sensors. *Front. Chem.* **2022**, *10*, 881172. [[CrossRef](#)] [[PubMed](#)]

26. Huang, P.; Wu, W.; Li, M.; Li, Z.; Pan, L.; Ahamad, T.; Alshehri, S.M.; Bando, Y.; Yamauchi, Y.; Xu, X. Metal-Organic Framework-Based Nanoarchitectonics: A Promising Material Platform for Electrochemical Detection of Organophosphorus Pesticides. *Coord. Chem. Rev.* **2024**, *501*, 215534. [[CrossRef](#)]
27. Song, M.-K.; Park, S.; Alamgir, F.M.; Cho, J.; Liu, M. Nanostructured Electrodes for Lithium-Ion and Lithium-Air Batteries: The Latest Developments, Challenges, and Perspectives. *Mater. Sci. Eng. R Rep.* **2011**, *72*, 203–252. [[CrossRef](#)]
28. Prasad, G.V.; Vinothkumar, V.; Jang, S.J.; Kim, T.H. An Ultra-Sensitive Electrochemical Sensor Based on MOF-Derived ZnO/Co₃O₄ Decorated on Graphene for Low-Level Monitoring of the α 1-AR Antagonist Alfuzosin in Tablets and Human Samples. *Inorg. Chem. Front.* **2023**, *10*, 4829–4844. [[CrossRef](#)]
29. Kitagawa, S. Metal–Organic Frameworks (MOFs). *Chem. Soc. Rev.* **2014**, *43*, 5415–5418.
30. Yin, Z.; Zhou, Y.-L.; Zeng, M.-H.; Kurmoo, M. The Concept of Mixed Organic Ligands in Metal–Organic Frameworks: Design, Tuning and Functions. *Dalton Trans.* **2015**, *44*, 5258–5275. [[CrossRef](#)] [[PubMed](#)]
31. Mason, J.A.; Veenstra, M.; Long, J.R. Evaluating Metal–Organic Frameworks for Natural Gas Storage. *Chem. Sci.* **2014**, *5*, 32–51. [[CrossRef](#)]
32. Mahmoud, E.; Ali, L.; El Sayah, A.; Alkhatib, S.A.; Abdulsalam, H.; Juma, M.; Al-Muhtaseb, A.H. Implementing Metal-Organic Frameworks for Natural Gas Storage. *Crystals* **2019**, *9*, 406. [[CrossRef](#)]
33. Farrusseng, D. *Metal-Organic Frameworks: Applications from Catalysis to Gas Storage*; John Wiley & Sons: Hoboken, NJ, USA, 2011.
34. Qiu, S.; Xue, M.; Zhu, G. Metal–Organic Framework Membranes: From Synthesis to Separation Application. *Chem. Soc. Rev.* **2014**, *43*, 6116–6140. [[CrossRef](#)]
35. Zhao, X.; Wang, Y.; Li, D.; Bu, X.; Feng, P. Metal–Organic Frameworks for Separation. *Adv. Mater.* **2018**, *30*, 1705189. [[CrossRef](#)] [[PubMed](#)]
36. Li, J.-R.; Sculley, J.; Zhou, H.-C. Metal–Organic Frameworks for Separations. *Chem. Rev.* **2012**, *112*, 869–932. [[CrossRef](#)] [[PubMed](#)]
37. Shen, K.; Chen, X.; Chen, J.; Li, Y. Development of MOF-Derived Carbon-Based Nanomaterials for Efficient Catalysis. *ACS Catal.* **2016**, *6*, 5887–5903. [[CrossRef](#)]
38. Li, Y.; Xie, M.; Zhang, X.; Liu, Q.; Lin, D.; Xu, C.; Xie, F.; Sun, X. Co-MOF Nanosheet Array: A High-Performance Electrochemical Sensor for Non-Enzymatic Glucose Detection. *Sens. Actuators B Chem.* **2019**, *278*, 126–132. [[CrossRef](#)]
39. Kajal, N.; Singh, V.; Gupta, R.; Gautam, S. Metal Organic Frameworks for Electrochemical Sensor Applications: A Review. *Environ. Res.* **2022**, *204*, 112320. [[CrossRef](#)] [[PubMed](#)]
40. Gonçalves, J.M.; Martins, P.R.; Rocha, D.P.; Matias, T.A.; Juliao, M.S.; Munoz, R.A.; Angnes, L. Recent Trends and Perspectives in Electrochemical Sensors Based on MOF-Derived Materials. *J. Mater. Chem. C* **2021**, *9*, 8718–8745. [[CrossRef](#)]
41. Lin, R.-B.; Zhang, Z.; Chen, B. Achieving High Performance Metal–Organic Framework Materials through Pore Engineering. *Acc. Chem. Res.* **2021**, *54*, 3362–3376. [[CrossRef](#)] [[PubMed](#)]
42. Ji, Z.; Wang, H.; Canossa, S.; Wuttke, S.; Yaghi, O.M. Pore Chemistry of Metal–Organic Frameworks. *Adv. Funct. Mater.* **2020**, *30*, 2000238. [[CrossRef](#)]
43. Senkowska, I.; Kaskel, S. Ultrahigh Porosity in Mesoporous MOFs: Promises and Limitations. *Chem. Commun.* **2014**, *50*, 7089–7098. [[CrossRef](#)] [[PubMed](#)]
44. Kim, T.K.; Lee, K.J.; Cheon, J.Y.; Lee, J.H.; Joo, S.H.; Moon, H.R. Nanoporous Metal Oxides with Tunable and Nanocrystalline Frameworks via Conversion of Metal–Organic Frameworks. *J. Am. Chem. Soc.* **2013**, *135*, 8940–8946. [[CrossRef](#)] [[PubMed](#)]
45. Guan, C.; Liu, X.; Elshahawy, A.M.; Zhang, H.; Wu, H.; Pennycook, S.J.; Wang, J. Metal–Organic Framework Derived Hollow CoS₂ Nanotube Arrays: An Efficient Bifunctional Electrocatalyst for Overall Water Splitting. *Nanoscale Horiz.* **2017**, *2*, 342–348. [[CrossRef](#)] [[PubMed](#)]
46. Zhao, S.; Yin, H.; Du, L.; He, L.; Zhao, K.; Chang, L.; Yin, G.; Zhao, H.; Liu, S.; Tang, Z. Carbonized Nanoscale Metal–Organic Frameworks as High Performance Electrocatalyst for Oxygen Reduction Reaction. *ACS Nano* **2014**, *8*, 12660–12668. [[CrossRef](#)] [[PubMed](#)]
47. Zhang, Q.; Xue, C.; Wang, J.; Huang, R.; Hao, X.; Li, K. Research Progress on Nanoporous Carbons Produced by the Carbonization of Metal Organic Frameworks. *New Carbon Mater.* **2021**, *36*, 322–335. [[CrossRef](#)]
48. Park, J.; Shen, X.; Wang, G. Solvothermal Synthesis and Gas-Sensing Performance of Co₃O₄ Hollow Nanospheres. *Sens. Actuators B Chem.* **2009**, *136*, 494–498. [[CrossRef](#)]
49. Xu, J.M.; Cheng, J.P. The Advances of Co₃O₄ as Gas Sensing Materials: A Review. *J. Alloys Compd.* **2016**, *686*, 753–768. [[CrossRef](#)]
50. Wu, X.; Han, Z.; Zheng, X.; Yao, S.; Yang, X.; Zhai, T. Core-Shell Structured Co₃O₄@NiCo₂O₄ Electrodes Grown on Flexible Carbon Fibers with Superior Electrochemical Properties. *Nano Energy* **2017**, *31*, 410–417. [[CrossRef](#)]
51. Wang, Y.; Che, P.; Du, X.; Zhang, X. Three-Dimensional Co₃O₄@NiCo₂O₄ Nanoarrays with Different Morphologies as Electrocatalysts for Oxygen Evolution Reaction. *Int. J. Hydrog. Energy* **2020**, *45*, 28598–28606. [[CrossRef](#)]
52. Xue, B.; Li, K.; Feng, L.; Lu, J.; Zhang, L. Graphene Wrapped Porous Co₃O₄/NiCo₂O₄ Double-Shelled Nanocages with Enhanced Electrocatalytic Performance for Glucose Sensor. *Electrochimica Acta* **2017**, *239*, 36–44. [[CrossRef](#)]
53. Sudha, V.; Senthil Kumar, S.M.; Thangamuthu, R. NiCo₂O₄ Nanorod: Synthesis and Electrochemical Sensing of Carcinogenic Hydrazine. *Inorg. Chem. Commun.* **2020**, *116*, 107927. [[CrossRef](#)]
54. Haseba, A.A.; Mohameda, G.G.; Elasherya, S.E. Potentiometric Determination of Alfuzosin Hydrochloride in Pharmaceutical Preparations and Biological Fluids Using Modified Carbon Paste Electrodes. *J. Basic Environ. Sci.* **2019**, *6*, 318–323.

55. Hadad, G.M.; Emara, S.; Mahmoud, W.M. Development and Validation of a Stability-Indicating RP-HPLC Method for the Determination of Paracetamol with Dantralone or/and Cetirizine and Pseudoephedrine in Two Pharmaceutical Dosage Forms. *Talanta* **2009**, *79*, 1360–1367. [[CrossRef](#)] [[PubMed](#)]
56. Attia, K.A.; El-Abasawi, N.M.; Abdelazim, A.H. Colorimetric Estimation of Alfuzosin Hydrochloride in Pharmaceutical Preparation Based on Computational Studies. *Anal. Methods* **2016**, *8*, 1798–1805. [[CrossRef](#)]
57. Baezzat, M.R.; Banavand, F.; Fasihi, F. Electrooxidation Study and Highly Sensitive Voltammetric Determination of Alfuzosin Employing Multi-Walled Carbon Nanotubes and the Ionic Liquid 1-Hexylpyridinium Hexafluorophosphate Nanocomposite Sensor. *J. Mol. Liq.* **2017**, *233*, 391–397. [[CrossRef](#)]
58. Qian, J.; Sun, F.; Qin, L. Hydrothermal Synthesis of Zeolitic Imidazolate Framework-67 (ZIF-67) Nanocrystals. *Mater. Lett.* **2012**, *82*, 220–223. [[CrossRef](#)]
59. Hou, W.; Huang, Y.; Liu, X. Highly Efficient and Recyclable ZIF-67 Catalyst for the Degradation of Tetracycline. *Catal. Lett.* **2020**, *150*, 3017–3022. [[CrossRef](#)]
60. Guan, D.; Zhong, J.; Xu, H.; Huang, Y.-C.; Hu, Z.; Chen, B.; Zhang, Y.; Ni, M.; Xu, X.; Zhou, W.; et al. A Universal Chemical-Induced Tensile Strain Tuning Strategy to Boost Oxygen-Evolving Electrocatalysis on Perovskite Oxides. *Appl. Phys. Rev.* **2022**, *9*, 011422. [[CrossRef](#)]
61. Kim: Analysis of the NiCo₂O₄ Spinel Surface with Auger and X-ray Photoelectron Spectroscopy. Available online: https://scholar.google.com/scholar_lookup?title=Analysis%20of%20the%20NiCo2O4%20spinel%20surface%20with%20Auger%20and%20X-ray%20photoelectron%20spectroscopy&publication_year=2000&author=J.G.%20Kim&author=D.L.%20Pugmire&author=D.%20Battaglia&author=M.A.%20Langell (accessed on 14 April 2024).
62. Marco: Characterization of the Nickel Cobaltite, NiCo₂O₄, Prepared by Several Methods: An XRD, XANES, EXAFS, and XPS Study. Available online: https://scholar.google.com/scholar_lookup?title=Characterization%20of%20the%20nickel%20cobaltite,%20NiCo2O4,%20prepared%20by%20several%20methods:%20an%20XRD,%20XANES,%20EXAFS,%20and%20XPS%20study&publication_year=2000&author=J.F.%20Marco&author=J.R.%20Gancedo&author=M.%20Gracia&author=J.L.%20Gautier&author=E.%20R%C3%ADos&author=F.J.%20Berry (accessed on 14 April 2024).
63. Yuan, C.; Li, J.; Hou, L.; Yang, L.; Shen, L.; Zhang, X. Facile Template-Free Synthesis of Ultralayered Mesoporous Nickel Cobaltite Nanowires towards High-Performance Electrochemical Capacitors. *J. Mater. Chem.* **2012**, *22*, 16084–16090. [[CrossRef](#)]
64. Dupin, J.-C.; Gonbeau, D.; Vinatier, P.; Levasseur, A. Systematic XPS Studies of Metal Oxides, Hydroxides and Peroxides. *Phys. Chem. Chem. Phys.* **2000**, *2*, 1319–1324. [[CrossRef](#)]
65. An, C.; Wang, Y.; Huang, Y.; Xu, Y.; Xu, C.; Jiao, L.; Yuan, H. Novel Three-Dimensional NiCo₂O₄ Hierarchitectures: Solvothermal Synthesis and Electrochemical Properties. *CrystEngComm* **2014**, *16*, 385–392. [[CrossRef](#)]
66. Zhang, H.; Guan, D.; Gu, Y.; Xu, H.; Wang, C.; Shao, Z.; Guo, Y. Tuning Synergy between Nickel and Iron in Ruddlesden–Popper Perovskites through Controllable Crystal Dimensionalities towards Enhanced Oxygen-Evolving Activity and Stability. *Carbon Energy* **2024**, e465. [[CrossRef](#)]
67. Budi, C.S.; Deka, J.R.; Hsu, W.-C.; Saikia, D.; Chen, K.-T.; Kao, H.-M.; Yang, Y.-C. Bimetallic Co/Zn Zeolitic Imidazolate Framework ZIF-67 Supported Cu Nanoparticles: An Excellent Catalyst for Reduction of Synthetic Dyes and Nitroarenes. *J. Hazard. Mater.* **2021**, *407*, 124392. [[CrossRef](#)] [[PubMed](#)]
68. Mohtasham, H.; Rostami, M.; Gholipour, B.; Sorouri, A.M.; Ehrlich, H.; Ganjali, M.R.; Rostamnia, S.; Rahimi-Nasrabadi, M.; Salimi, A.; Luque, R. Nano-Architecture of MOF (ZIF-67)-Based Co₃O₄ NPs@N-Doped Porous Carbon Polyhedral Nanocomposites for Oxidative Degradation of Antibiotic Sulfamethoxazole from Wastewater. *Chemosphere* **2023**, *310*, 136625. [[CrossRef](#)] [[PubMed](#)]
69. Guo, C.; Guo, J.; Zhang, Y.; Wang, D.; Zhang, L.; Guo, Y.; Ma, W.; Wang, J. Synthesis of Core–Shell ZIF-67@Co-MOF-74 Catalyst with Controllable Shell Thickness and Enhanced Photocatalytic Activity for Visible Light-Driven Water Oxidation. *CrystEngComm* **2018**, *20*, 7659–7665. [[CrossRef](#)]
70. Venu Gopal, T.; Reddy, T.M.; Venkataprasad, G.; Shaikshavalli, P.; Gopal, P. Rapid and Sensitive Electrochemical Monitoring of Paracetamol and Its Simultaneous Resolution in Presence of Epinephrine and Tyrosine at GO/Poly(Val) Composite Modified Carbon Paste Electrode. *Colloids Surf. Physicochem. Eng. Asp.* **2018**, *545*, 117–126. [[CrossRef](#)]
71. Prasad, G.V.; Jang, S.-J.; Sekhar, Y.C.; Reddy, T.M.; Sarma, L.S.; Kim, H.-B.; Kim, T.H. Fine-Tuning of Pd–CeO₂/rGO Nanocomposite: A Facile Synergetic Strategy for Effective Electrochemical Detection of Dopamine in Pharmaceutical and Biological Samples. *J. Electroanal. Chem.* **2023**, *941*, 117544. [[CrossRef](#)]

Disclaimer/Publisher’s Note: The statements, opinions and data contained in all publications are solely those of the individual author(s) and contributor(s) and not of MDPI and/or the editor(s). MDPI and/or the editor(s) disclaim responsibility for any injury to people or property resulting from any ideas, methods, instructions or products referred to in the content.